4D imaging of fracturing in organic-rich shales during heating

Maya Kobchenko, Hamed Panahi, François Renard, Dag K. Dysthe, Anders Malthe-Sørenssen, Adriano Mazzini, Julien Scheibert, Bjorn Jamtveit, Paul Meakin

▶ **To cite this version:**

Maya Kobchenko, Hamed Panahi, François Renard, Dag K. Dysthe, Anders Malthe-Sørenssen, et al.. 4D imaging of fracturing in organic-rich shales during heating. Journal of Geophysical Research : Solid Earth, 2011, 116, pp.B12201. 10.1029/2011JB008565 . insu-00680815

HAL Id: insu-00680815
https://insu.hal.science/insu-00680815

Submitted on 2 Mar 2021

HAL is a multi-disciplinary open access archive for the deposit and dissemination of scientific research documents, whether they are published or not. The documents may come from teaching and research institutions in France or abroad, or from public or private research centers.

L'archive ouverte pluridisciplinaire **HAL**, est destinée au dépôt et à la diffusion de documents scientifiques de niveau recherche, publiés ou non, émanant des établissements d'enseignement et de recherche français ou étrangers, des laboratoires publics ou privés.

4D imaging of fracturing in organic-rich shales during heating

Maya Kobchenko,[1] Hamed Panahi,[1,2] François Renard,[1,3] Dag K. Dysthe,[1] Anders Malthe-Sørenssen,[1] Adriano Mazzini,[1] Julien Scheibert,[1,4] Bjørn Jamtveit,[1] and Paul Meakin[1,5,6]

Received 1 June 2011; revised 12 September 2011; accepted 16 September 2011; published 7 December 2011.

[1] To better understand the mechanisms of fracture pattern development and fluid escape in low permeability rocks, we performed time-resolved in situ X-ray tomography imaging to investigate the processes that occur during the slow heating (from 60° to 400°C) of organic-rich Green River shale. At about 350°C cracks nucleated in the sample, and as the temperature continued to increase, these cracks propagated parallel to shale bedding and coalesced, thus cutting across the sample. Thermogravimetry and gas chromatography revealed that the fracturing occurring at ∼350°C was associated with significant mass loss and release of light hydrocarbons generated by the decomposition of immature organic matter. Kerogen decomposition is thought to cause an internal pressure build up sufficient to form cracks in the shale, thus providing pathways for the outgoing hydrocarbons. We show that a 2D numerical model based on this idea qualitatively reproduces the experimentally observed dynamics of crack nucleation, growth and coalescence, as well as the irregular outlines of the cracks. Our results provide a new description of fracture pattern formation in low permeability shales.

Citation: Kobchenko, M., H. Panahi, F. Renard, D. K. Dysthe, A. Malthe-Sørenssen, A. Mazzini, J. Scheibert, B. Jamtveit, and P. Meakin (2011), 4D imaging of fracturing in organic-rich shales during heating, *J. Geophys. Res.*, *116*, B12201, doi:10.1029/2011JB008565.

1. Introduction

[2] A wide variety of geological phenomena involve the generation and migration of fluids in low permeability rocks. For example, dehydration of sediments in subduction zones generates large fluxes of water that rise along low-permeability subduction interfaces, and provide a mechanism for creep and/or slow earthquakes [*Obara*, 2002]. Similarly, the illitization of clays at depth and the production of methane in organic-rich shales were suggested to contribute to the development of overpressure and the formation of piercement structures, which are manifest on the surface as mud volcanoes [*Mazzini*, 2009]. Also, the emplacement of magmatic bodies into sedimentary basins induces rapid decomposition of organic matter, and the resulting gases migrate through low permeability rocks in quantities that may significantly alter the climate [*Svensen et al.*, 2004]. In all these geological systems, the migration of a fluid through low permeability rocks is coupled with deformation. This type of coupling between fluid flow and deformation is also important in the primary migration of hydrocarbons.

[3] Primary migration is the transport of hydrocarbon fluids from extremely low permeability source rocks, in which they are generated, to more permeable rocks through which they migrate to a trap (reservoir) or to the surface. This natural process is of both economic and fundamental interest. As the organic-rich fine grained sediment from which the source rock is formed is buried, the organic material is transformed into complex high molecular weight/cross-linked organic oil and gas precursors (kerogen). As the burial depth increases, the temperature and pressure rise, and kerogen decomposes into low molecular weight hydrocarbon fluids (gas and oil), which have much lower viscosities than the kerogen. The generated hydrocarbon fluids escape from the shale into secondary migration pathways, by processes that remain enigmatic, in spite of decades of investigation [*Bjørlykke*, 2010].

[4] Fracturing is commonly cited as a likely mechanism to increase the permeability of source rocks and provide pathways for the generated hydrocarbons [*Berg and Gangi*, 1999; *Lash and Engelder*, 2005]. During kerogen decomposition, generation of less dense fluids leads to pore pressure build-up, which may cause fracturing of the host rock. The presence of microcracks is commonly observed in thin sections of recovered source rock samples [*Capuano*, 1993; *Marquez and Mountjoy*, 1996; *Lash and Engelder*, 2005],

[1]Physics of Geological Processes, University of Oslo, Oslo, Norway.
[2]Statoil ASA, Oslo, Norway.
[3]Institut des Sciences de la Terre, Université Joseph Fourier, CNRS, Grenoble, France.
[4]Laboratoire de Tribologie et Dynamique des Systèmes, CNRS, Ecole Centrale de Lyon, Ecully CEDEX, France.
[5]Center for Advanced Modeling and Simulation, Idaho National Laboratory, Idaho Falls, Idaho, USA.
[6]Institute for Energy Technology, Kjeller, Norway.

Copyright 2011 by the American Geophysical Union.
0148-0227/11/2011JB008565

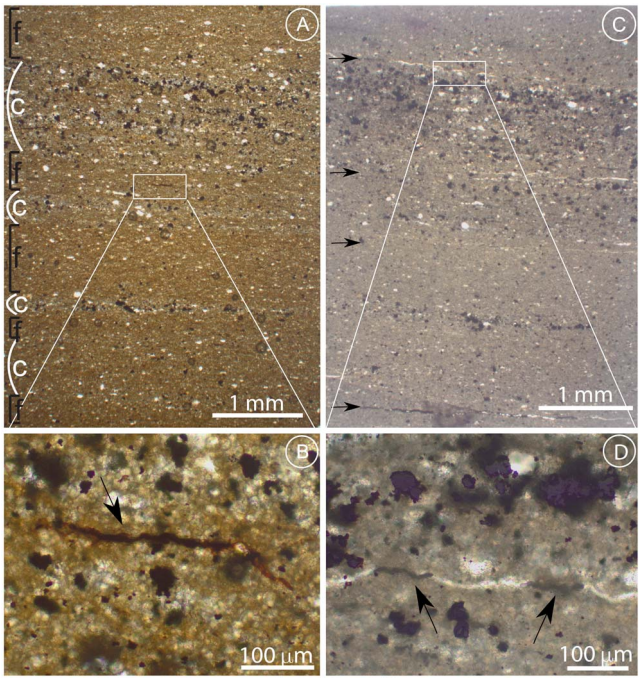

Figure 1. Thin section images of Green River Shale sample before and after heating. (a) Interlaminated silt and clay-rich layers before heating. Here f indicates clay-rich layers with a higher amount of kerogen lenses and c indicates coarser layers with siliciclastic grains. (b) Detail of a kerogen lens. (c) Image of the same sample after heating. Arrows indicate the position of cracks developed during heating. Fractures propagated mainly in the finer grained intervals where the highest concentration of organic matter lenses was also observed. (d) Detail of a crack filled with organic remains (arrows).

suggesting that microcracks may be involved in fluid migration.

[5] Under natural conditions, this fracture process takes place at depths of several kilometers over millions of years, making its monitoring impossible. Therefore, it is very important to construct adequate models of primary migration. Several theoretical and numerical studies of fracture formation in organic-rich shales have been described in the scientific literature [*Ozkaya*, 1988; *Jin et al.*, 2010]. *Jin et al.* [2010] introduced a fracture mechanics model of subcritical crack propagation and coalescence, based on the assumption of linear elastic behavior of the rock. Although the model provides an estimate of the fracture propagation time, the 3D geometry and mechanism of fracture formation in heterogeneous shale remain unclear.

[6] To better understand the complex phenomenon of hydrocarbon expulsion from very low permeability source rock, we employed a new experimental approach – real-time 3D X-ray tomography – during gradual heating of a shale sample coupled with thermogravimetry and petrography analyses before and after heating. This study included only unconfined samples, but it is an important step toward the goal of unraveling the numerous and complex mechanisms controlling primary migration.

2. Characterization of Green River Shale Samples

[7] The samples were obtained from an outcrop of the organic-rich R-8 unit of the Green River Shale Formation (Piceance Basin, northwestern Colorado). The formation consists of Eocene lacustrine marl/silt sediments [*Ruble et al.*, 2001] with well-developed lamination and anisotropic mechanical properties [*Vernik and Landis*, 1996]. It contains organic matter (total organic content = 9.92 wt% in analyzed samples) present in the form of patches of kerogen, preferentially distributed parallel to the bedding (Figures 1a and 1b). This part of the formation has never been buried deeply enough to reach temperatures sufficient to cause significant thermal maturation.

[8] Cylindrical core samples (5 mm height, 5 mm in diameter) cut perpendicular to the bedding were prepared for X-ray tomography. Thin sections were taken before and after heating. Optical microscope images (Figures 1a and 1b) highlight the micro-fabric of the uncooked shale consisting of alternating lamellae of: coarser and lighter colored carbonate cemented layers rich in siliciclastic grains (e.g., quartz) and pyrite framboids; and darker and finer grained clay-rich layers, containing greater amount of discontinuous organic matter lenses.

3. 4D Imaging and Data Processing

[9] Time-lapse X-ray tomography 3D imaging of the shale samples was carried out using beamline ID19 at the European Synchrotron Radiation Facility in Grenoble, France. This non-invasive imaging technique measures the absorption of X-rays, to produce a 3D attenuation map.

[10] The prepared shale cylinder was placed in a home-built furnace in contact with air, with no confining pressure, and it was gradually heated in situ from 60°C to 400°C at approximately 1°C/min. 68 3D scans of this sample were taken, of which 28 were acquired during the heating phase and the rest at 400°C. For all scans, 1500 radiographs were acquired while the sample was rotated over 180°. The beam energy of 20 keV allowed images to be captured with a spatial resolution of 5 μm ($5 \times 5 \times 5$ μm^3 voxels) and a time resolution of 11–14 min per 3D scan. 3D raw-tomograms representing the microporous structure of the sample at different stages of heating were constructed from the X-ray data. The final volumes contained 830^3 voxels coded in 8-bit gray levels.

[11] The 3D images were processed in two ways. First, the strain field was measured in a typical 2D vertical slice of the volume, using digital image correlation [*Rechenmacher and Finno*, 2004; *Hild and Roux*, 2006; *Viggiani*, 2009; *Bornert et al.*, 2010]. Second, in order to determine crack geometries and track crack propagation, the shape, volume and morphology of the cracks were analyzed in 3D using the AvizoFire© software package. Quantitative analysis of the crack formation required isolation of the cracks from the rock matrix. Due to the small crack opening (4–5 voxels), the following procedure was applied: first a binary mask was used to delete the background; then an edge-preserving

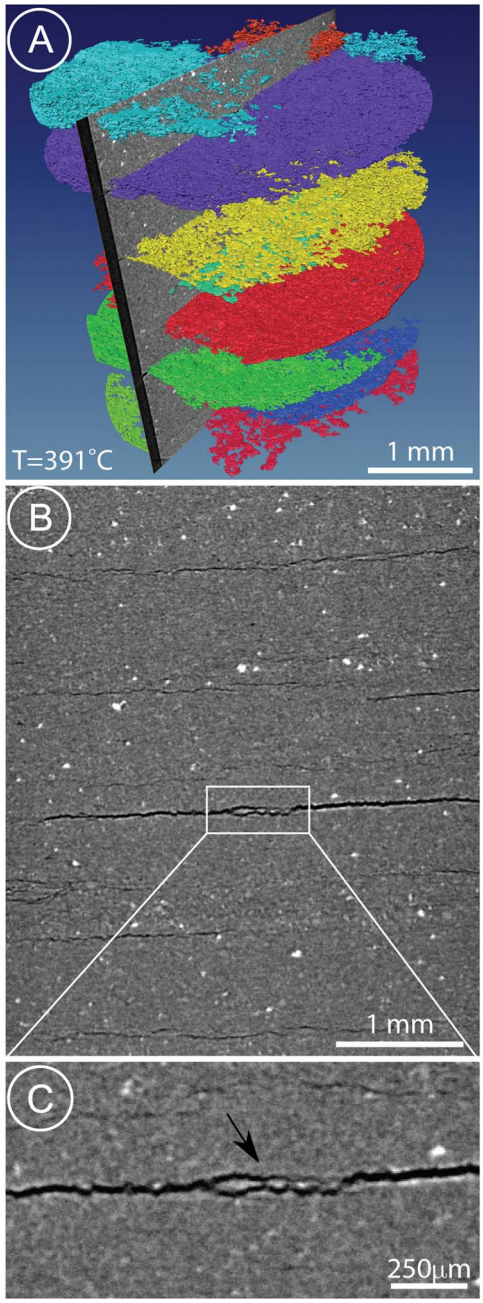

Figure 2. Tomography images of the shale sample at 391°C, corresponding to the moment of maximum crack opening. (a) 3D rendering of final crack network. Each color defines an independent crack. (b) 2D slice showing (dark color) elongated cracks that developed parallel to the bedding. (c) Detail of Figure 2b showing a crack developed around a pyrite grain (arrow).

smoothing filter based on Gaussian smoothing combined with a nonlinear diffusion algorithm was applied; then a "watershed" procedure enabled individual cracks to be isolated [*Sonka et al.*, 1999]. The final result of this segmentation procedure was a series of cracks consisting of connected voxels, marked by different labels/colors (Figure 2a and Animations S1 and S2 of the auxiliary material).[1]

4. Observation of Deformation and Crack Formation

[12] Correlation analysis and 3D image analysis were performed to determine the deformation of the sample before fracturing and the geometries of the developing cracks. The spatial fluctuations of the attenuation maps (see Figure 2b) served as markers when the digital correlation technique was used to compare successive images. To calculate the correlation matrix we used a correlation box of size 25 by 25 pixels (125 by 125 μm^2), which enabled us to measure the spatial distribution of micro-displacements.

[13] Between room temperature and 300°C, the shale dilated anisotropically in the vertical (perpendicular to the shale bedding) and horizontal (parallel to the shale bedding) directions, and the strain curves showed a quasi-linear increase with temperature, as expected for linear thermal expansion (Figure 3a). The coefficient for thermal expansion was determined to be 5.5 * 10^{-5}/°C in the vertical direction and 2.5 * 10^{-5}/°C in the horizontal direction, which clearly indicates the anisotropy of the shale, in agreement with other studies on the same shale [*Grebowicz*, 2008]. At 300°C, the vertical expansion started to deviate from linearity, which is likely related to the onset of organic degassing before crack formation. At a temperature of about 350°C the sample undergoes rapid localized deformation owing to fluid generation and the onset of fracturing. When the sample breaks, black structures corresponding to the newly formed cracks appear in the images (see Figure 2b), which have no equivalent in the preceding ones, thus ruining the correlation technique. Moreover, after the sample fractures, global movement of the sample occurs (translation and rotation), with displacements from one data set to the next of amplitude greater than 12 pixels, which was estimated to be the maximum displacement that can be accurately measured using the correlation technique. Even though the correlation results during and after fracturing are not trustworthy, this technique accurately determines the sample deformation before fracturing occurs.

[14] With 3D tomography, we imaged 3 stages of fracture propagation. The first microfracture pattern was detected at a temperature of about 350°C. Figure 2a shows a 3D rendering of the most opened fractures at T = 391°C (third time step) and Figures 2b and 2c show a vertical slice through the tomography image. The general direction of crack propagation followed the shale bedding, and no perpendicular fractures were observed (Figure 2b). Pyrite grains, observable as bright spots in the tomography images (Figure 2c), affected crack growth by pinning the crack front, and controlling the out-of-plane fluctuations of the crack path.

[15] The fractures can be described in terms of two rough, essentially parallel surfaces that enclose the fracture aperture. Both surfaces can be described by height functions, $h_1(x,y)$ and $h_2(x,y)$, where (x,y) is the position in the common plane. Figure 4a shows the topography of fracture surface $h_1(x,y)$, where the fluctuation of surface function

[1]Auxiliary materials are available in the HTML. doi:10.1029/2011JB008565.

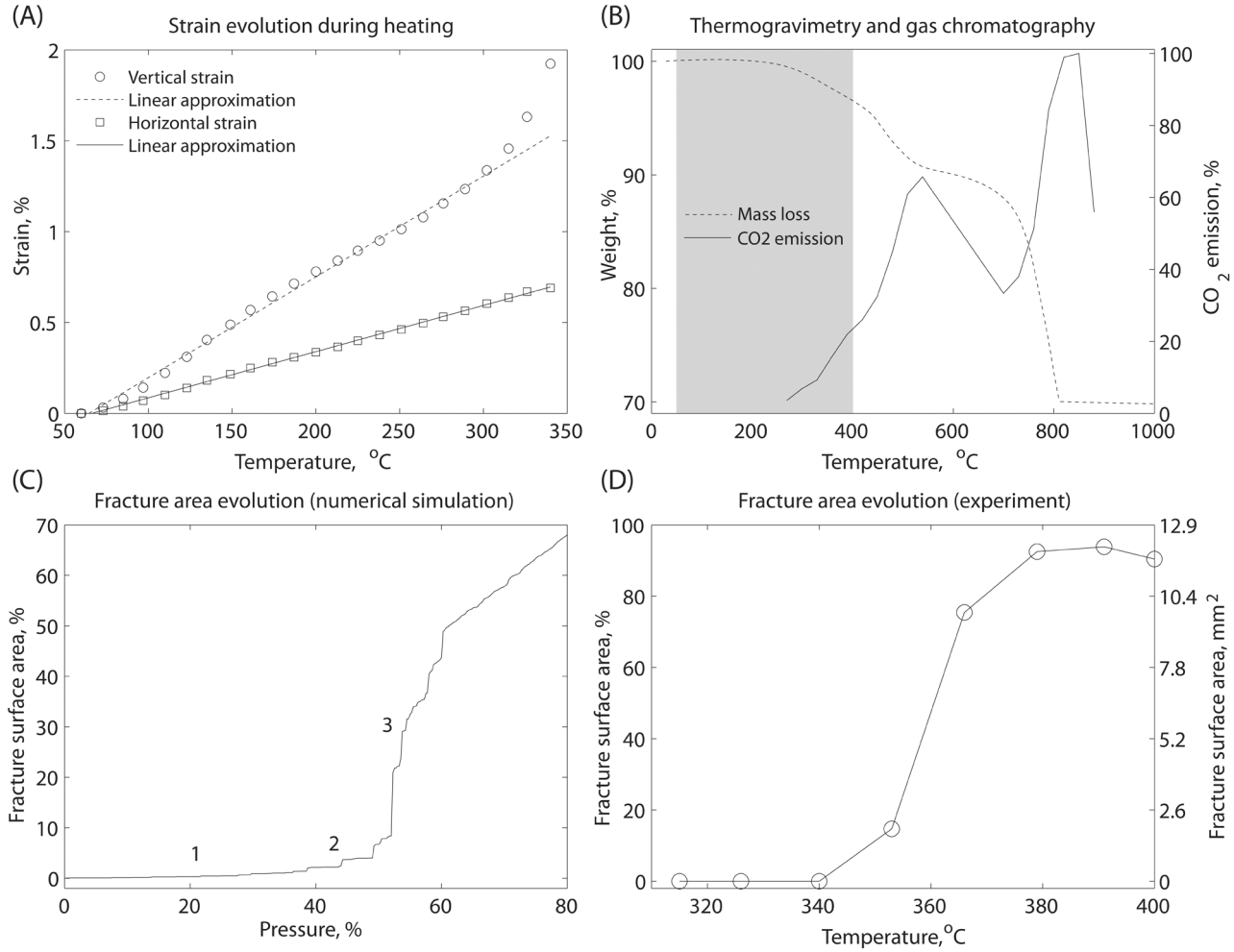

Figure 3. (a) Vertical and horizontal strain in a shale sample during heating. The linear relationship between 70°C and 300°C corresponds to dilation of the sample due to thermal expansion. Because of the anisotropy of the shale, the vertical and horizontal dilations are different. The vertical strain-temperature relationship deviates from linearity at 300°C, at the onset of degassing. Failure of the correlation technique at 350°C corresponds to the fracturing of the sample. (b) Thermogravimetry (mass loss) and carbon dioxide emission analyses in aerobic conditions. The change of slope on the mass loss curve at around 300°C occurs at the same temperature as the onset of CO_2 production and corresponds to the onset of kerogen decomposition. The gray shaded area indicates the temperature range of the tomography experiment. The peak of CO_2 production and mass loss at around 800°C corresponds to the decomposition of carbonate. (c) Growth of the area of the biggest crack as a function of pressure (% of maximum applied pressure) in the 2D lattice model. Numbers 1–3 are the three stages of crack evolution corresponding to nucleation, growth and coalescence (see corresponding snapshots 1–3 in Figure 5b). (d) Fracture evolution in the experiment. Growth of the surface area of the largest crack (in % of the sample cross-sectional area and in mm^2) as a function of temperature. The slight decrease of fracture surface area observed after 390°C is attributed to partial crack closing after fluid expulsion.

$h_1(x,y)$ around the flat plane (x,y) is indicated by the color code. Cracks have essentially constant aperture widths - the thickness function $h_2(x,y) - h_1(x,y)$ (4–5 pixels, i.e., 20–25 μm, see Figure 4b), and rough irregular outlines. The amplitude of the topography variation is around 10–15 pixels (i.e., 50–75 μm), as seen in the Figure 4a. The mid-plane ($H(x,y) = [h_1(x,y) + h_2(x,y)]/2$) is also rough, and it fluctuates about a flat plane – the "plane of the fracture." The projections of $h_1(x,y)$, $h_2(x,y)$ and $([h_1(x,y) + h_2(x,y)]/2$ into this plane, in a direction perpendicular to the plane, have a common shape, which consists of a continuous region with rough edges. When one fracture coalesces with another, a new fracture is formed, and it can be described in terms of the rough surfaces $H^{new}(x,y)$, $h_1^{new}(x,y)$ and $h_2^{new}(x,y)$. The projections of these rough surfaces are also a common shape, which consists of a continuous region with rough edges. The planes of the coalesced fracture and the two fractures that coalesced to form it are more-or-less parallel,

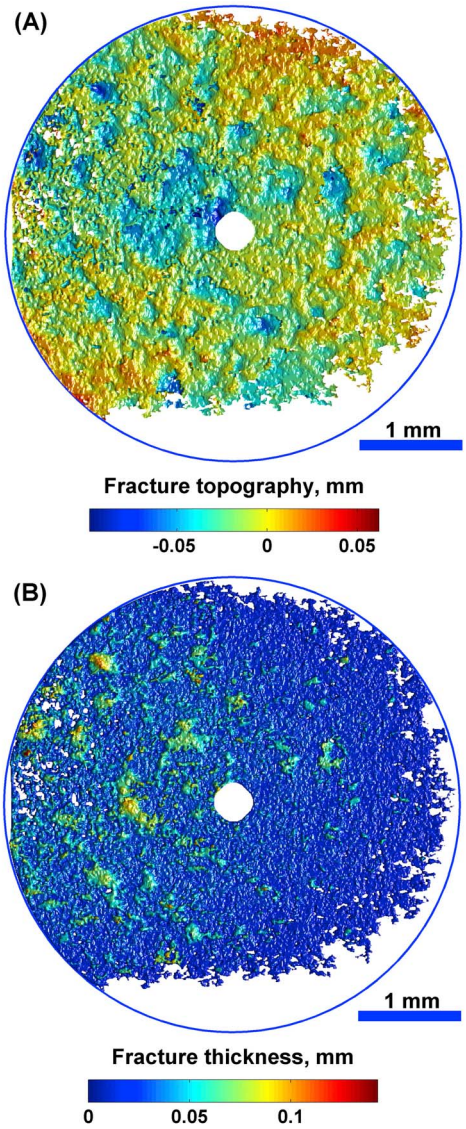

Figure 4. Reconstruction of the (a) topography and (b) thickness of a fracture extracted from Figure 2a. The circular central region in each image was removed because of a data acquisition artifact. The outer circle defines the boundaries of the sample. In Figure 4a fluctuation of fracture surface height $h_1(x,y)$ around the fracture plane (x,y) is indicated by the color scale. The fracture front is irregular. The topography is created by small heterogeneities (i.e., pyrite minerals) that pin the fracture during its propagation. In Figure 4b the fracture thickness, taken as the difference between the upper surface $h_1(x,y)$ and lower surface $h_2(x,y)$ of the fracture, is indicated by the color scale. The thickness is quasi-constant and it is perturbed by pyrite inclusions.

and also quasi-parallel to the shale lamination. Viewed from "above," in the direction perpendicular to the plane of the fractures and the lamination, the fractures are continuous, and they grow and coalesce in three successive stages (Figure 5a). As the temperature rose, cracks nucleated (1), grew and coalesced in a quasi-static manner (2) until they spanned the sample (3). The growth of the surface area of the biggest fracture with increasing temperature is shown in Figure 3d.

5. Organic Decomposition Induces Fracturing in the Shale

[16] Thin sections were studied in order to compare petrographic characteristics of the shale before and after heating. Before heating, organic precursors, which were preferentially oriented parallel to the shale bedding, could be distinguished throughout the sample (see Figures 1a and 1b). After heating, an abundance of cracks, partially filled with residual organic material, was distributed parallel to the bedding (Figures 1c and 1d). Petrographic observations revealed that cracks propagated mainly in the finer grained layers where the highest concentrations of organic matter lenses were observed (Figures 1a and 1c). The coarser grained layers, where quartz grains and pyrite framboids were present in higher concentration, also displayed better cementation with larger calcite crystals. The preferential location of fracture propagation is ascribed to two main factors: (1) Higher amounts of organic matter (kerogen lenses), which decomposes leading to fluid formation, internal pressure build up and eventually fracture initiation and propagation. (2) Finer grained intervals are less cemented than the coarser grained ones and they fracture more easily.

[17] The link between hydrocarbon generation and fracturing was tested using thermogravimetry and gas chromatography. Aerobic and anaerobic (nitrogen) thermogravimetry analyses on 500 mg samples were performed to investigate the presence of organic and inorganic carbon (carbonates) using a ATG/SDTA 851 Mettler Toledo apparatus. We monitored mass loss of the sample during heating at 10°C/min in air or nitrogen between 20°C and 1000°C. The loss of mass during heating occurred in distinct stages (Figure 3b), and the temperature range of each stage indicates the nature of the component that evaporates. We also used gas chromatography (GC 5890-MS 5973 Agilent) to analyze the gas that escaped (water, CO_2, and organic volatiles) during heating at a rate of 5°C/min in air. The first step of mass loss (Figure 3b) in the temperature range 300–450°C corresponds to the release of various organic molecules (alkanes, alkenes, toluene, xylenes), water and CO_2 (first peak on CO_2 emission plot) and indicates decomposition of organic matter. The second step of mass loss around 600–800°C indicates decomposition of carbonates. A similar behavior was observed when nitrogen was used instead of air with two peaks of CO_2 release located at the same temperatures.

[18] Figure 6 shows the correlations between strain evolution, mass loss, CO_2 emission and fracture surface area growth. Comparing the temperatures of degassing, mass loss and hydrocarbon release with the temperature of fracturing onset, we conclude that fracturing was induced by overpressure in the sample caused by organic matter decomposition.

6. Discrete Model of Crack Propagation

[19] Based on the experimentally observed fracturing behavior (Figure 5a), a two dimensional (2D) model of

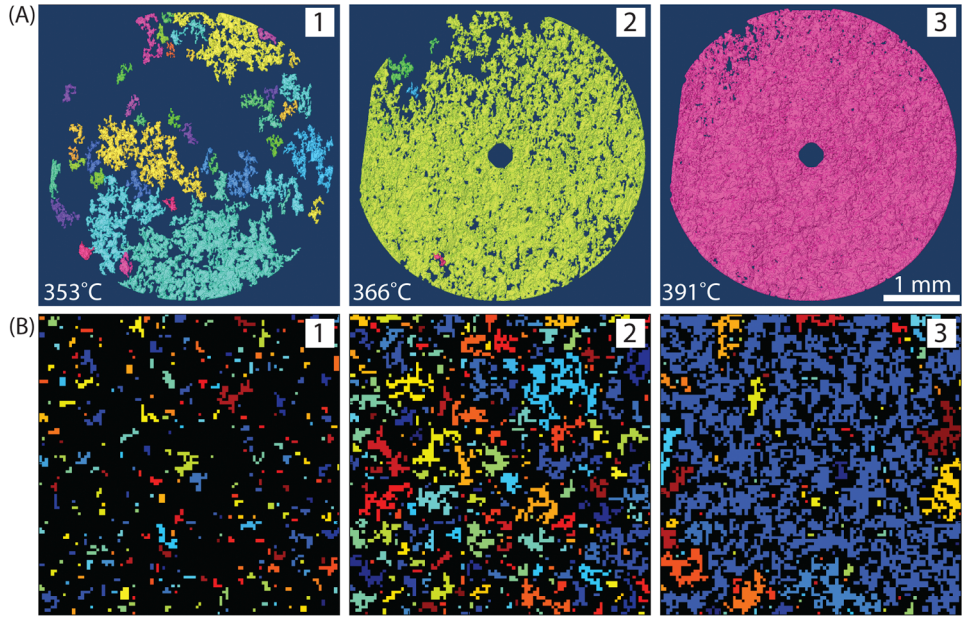

Figure 5. Comparison of crack evolution in the experiment and numerical model. (a) Crack propagation dynamics during heating in the experiment. View of the cracks in a kerogen rich layer viewed from a direction perpendicular to the average plane of the cracks. (1) Numerous small cracks nucleated at ~350°C. Each crack is indicated by a different color. (2) Cracks grew and merged with increasing temperature. (3) Ultimately all cracks merged into a single sample-wide crack. The circular central region in each image was removed because of a data acquisition artifact. (b) 2D lattice model at three stages of crack development: nucleation (1), growth (2) and coalescence (3) of cracks (see three stages of the area growth (1–3) in Figure 3c).

in-plane crack nucleation and growth due to internal pressure increase was developed (Figure 7). The choice of a 2D model is based on the observation of planar mode 1 cracks that follow the layering of the shale and the focus on in-plane dynamics rather than the placement of cracks and relation between cracks normal to their plane. To reproduce key characteristics of the crack growth process including the merging of small cracks and the very irregular crack shapes, we used a statistical fracture model [*Alava et al.*, 2006]. The main parameter needed is the variability of local strength, and the model neglects long range effects of the stress field. The model includes neither the kinetics of kerogen decomposition nor the elastic properties of the source rock, and therefore it cannot quantitatively predict threshold temperatures and pressures, or rates of primary migration. The objective of the model is to find the minimum number of features that explain the observed behavior. The macroscopic fracture threshold and kerogen transformation kinetics are important to predict at what temperature and rate these phenomena occur, but they do not help us understand how the fracture evolves. The percolation like evolution of the fracture, as opposed to the nucleation of a single fracture that propagates rapidly through the shale, which would be predicted by a macroscopic elastic model with a distributed pressure build-up, shows that the material disorder may cause the slow formation of percolating fluid pathways for expulsion of hydrocarbon fluids at pressures much smaller than those needed to completely fracture the shale. The model focuses on a layer of shale that fractures more rapidly than nearby layers because it has a higher kerogen content. The layer is modeled by using a regular square lattice in which every site represents a small organic-rich

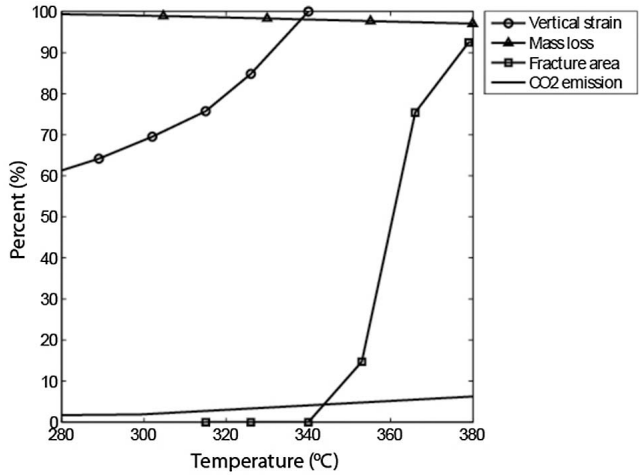

Figure 6. The correlation between vertical strain evolution (perpendicular to the shale lamination) during heating, mass loss, CO_2 emission and growth of fracture area in the shale sample. The onset of the mass loss and CO_2 emission corresponds to decomposition of organic material. The nonlinear strain growth in the vertical direction, which is caused by internal fluid pressure buildup, leads to the fracturing at 340°C.

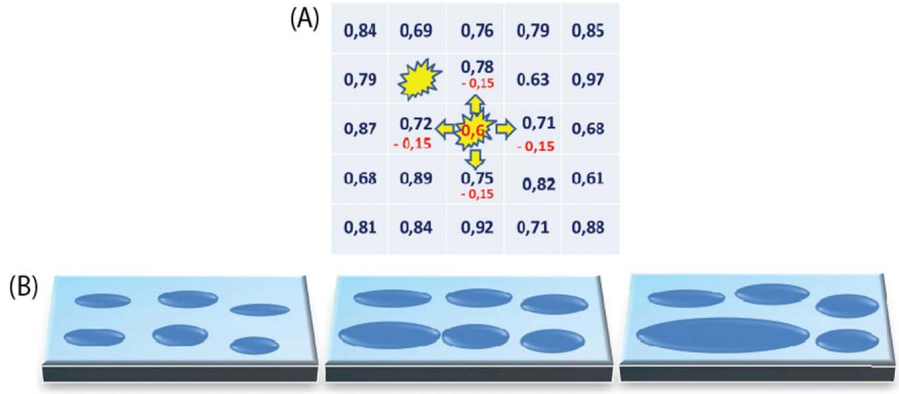

Figure 7. Sketch of the 2D discrete model. (a) The rock layer is modeled by a lattice of sites with assigned breaking thresholds. When a site fractures the stress is distributed equally to the non-broken neighbors, bringing them closer to failure. Two fractured neighbors are called a continuous crack. (b) The cracks grow by including new neighboring broken sites. When two cracks coalesce they form a bigger crack.

shale element. Each site is characterized by a randomly assigned breaking threshold $\sigma_{c,i}$. The pressure in the lattice rises incrementally during each time step and, when it exceeds the breaking threshold ($p_i > \sigma_{c,i}$), the site fractures to represent either nucleation of a new crack or growth of a pre-existing crack. This relaxes the stress, which is distributed equally to the nearest non-broken neighbors (long-range elastic interactions are neglected), bringing them closer to failure. The distribution of stress was implemented by reducing the breaking threshold, $\sigma_{c,i} \rightarrow \sigma_{c,i} - d\sigma$, for all nearest non-broken neighbors. Dimensionless units were used for the pressure and breaking thresholds. Each crack is represented by a cluster of broken sites. As soon as sites belonging to different clusters become adjacent, both clusters are merged to form a single crack, and all the merged sites are given the same label/color.

[20] Figure 5b shows three successive snapshots during a simulation. In the early stage, the system contains many small independent cracks. Each crack has a rough front, and over time, individual cracks grow slowly and merge until the whole plane is covered. Figure 3c displays the increase of the area of the crack that was the largest at the end of the simulation. Crack growth occurs in three stages: (1) the microcracks are all separated and their surface areas grow gradually; (2) the cracks start to coalesce, the rate at which the fractured area increases accelerates, and growth in the total fracture area is dominated by distinct jumps; and (3) ultimately the system is dominated by one large fracture, with an area that grows by intermittent increases (see also the corresponding snapshots 1–3 in Figure 5b and Animation S3 of the auxiliary material). The qualitative trend of the fracture area growth in the simulation (Figure 3c) is similar to that observed in the experiment (Figure 3d).

[21] The model is similar to the fiber bundle model with local load sharing, which has been intensively used to model material failure [*Pradhan et al.*, 2010]. We suggest that it can be applied to other geological systems in which chemical reactions induce volume increase and stress build-up in rocks. These systems are widespread and include, apart from primary migration of hydrocarbons, weathering of rocks near the surface [*Røyne et al.*, 2008] and dehydration of serpentines in subduction zones [*Jung*, 2004].

7. Discussion and Conclusion

[22] Time-resolved high-resolution synchrotron X-rays tomography was performed during gradual heating (from 60 to 400°C) of organic-rich immature shales. At 350°C the nucleation of many small cracks was detected. With further temperature increase these microcracks propagated parallel to the shale bedding, coalesced and ultimately spanned the whole sample.

[23] The central point of our work is the observed correlation between hydrocarbon expulsion and fracturing within the sample. To do this, we combined thermogravimetry, gas chromatography, strain analysis and 3D observation of fracture formation and analyze the data in 3 steps:

[24] 1. Analyzing tomograms, we found that fracturing begins at a temperature of about 350°C.

[25] 2. Using thermogravimetry, we determined that the sample started to loose mass in the same temperature range (about 350°C). This alone does not provide us with the composition of the lost material.

[26] 3. Using gas chromatography, we determine that the gases expelled at temperatures near 350°C were mainly oxidized hydrocarbons, and we conclude that they originate from kerogen decomposition.

[27] In the literature, some shale rocks are reported to contain horizontal (in the direction of shale bedding) mode I fractures as well as vertical (perpendicular to the shale bedding) fractures. The presence of vertical fractures indicates that the maximum stress is vertical [*Olson*, 1980; *Smith and Chong*, 1984]. However, at shallow depths, where the magnitudes of both the vertical and horizontal stresses are similar, horizontal hydro-fractures of significant lateral extent can be created due to anisotropy of shales [*Thomas*, 1972; *Jensen*, 1979]. Horizontal fractures are also observed to develop in clay-rich shales in response to high overpressures during maturation [*Littke et al.*, 1988], even in regions where the vertical stress is larger than the horizontal stress. The reason for this is thought to be the strong

lamination of these shales [*Lash and Engelder*, 2005]. Theoretical studies [*Ozkaya*, 1988] also showed that vertical cracks are unlikely to form by oil generation and the excess of oil pressure is sufficient to cause lateral fracturing if the aspect ratio of kerogen patches is sufficiently large.

[28] In nature petroleum generation takes place in the 80–150°C temperature range, and this occurs typically over time periods of 1–100 million years (up to 500 million in some geological situations). The heating rate for a basin like the North Sea is 1–2°C/million years, but during rapid sedimentation and subsidence the heating rate is as high as 10°C/million years [*Bjørlykke*, 2010]. In our experiments, conducted in a much shorter time, fracturing was observed to occur in the temperature range of 300–400°C.

[29] The decomposition of kerogen involves a very large number of coupled chemical reactions, and a temperature dependent rate constant is associated with each reaction. In general, the rates of these reactions can be represented approximately by the Arrhenius function $K_i = A_i T^n exp(-E_i^a/RT)$, where K_i is the rate constant for the ith reaction, A_i is its frequency factor, E_i^a is its activation energy, R is the gas constant and T is the absolute temperature. In most cases, n is small, the temperature dependence is dominated by the exponential term and the Arrhenius equation is often expressed in the form $A_i' exp(-E_i^a/RT)$. The overall rate of the organic maturation process, K, can also be represented by a similar Arrhenius function $K = Aexp(-E^a/RT)$, although the nature of the decomposition products is also somewhat temperature dependent. If the activation energy, E^a, is large enough, the maturation rate increases rapidly with increasing temperature, and this explains why a higher temperature can be used to accelerate the maturation process and achieve a maturation time that is short enough to conduct laboratory experiments.

[30] Under natural conditions cracks form during maturation at lower temperature, and because of the low rate of pressure buildup crack growth is probably a slow subcritical fracturing process. Based on theoretical calculations by [*Ozkaya*, 1988], we can estimate the conditions for the initiation of lateral cracking. [*Ozkaya*, 1988] considered a linearly elastic and isotropic source rock containing isolated kerogen flakes enclosed in an impermeable shale matrix, and showed that the aspect ratio of the kerogen particles may influence the initiation of horizontal microcracks in the source rock beds under maximum vertical principal stress. Initiation of microcracks as a function of kerogen flakes shape occurs when:

$$\Delta P\left(\frac{2w}{h} - 1\right) > S_v(2 - k) + C, \qquad (1)$$

where S_v is the principal vertical stress, k is the lateral to vertical stress ratio, C is the strength of the rock, ΔP is the excess oil pressure induced during kerogen decomposition, w is the characteristic length of the kerogen particles, and h is the thickness of kerogen particles. For example, for the kerogen patch shown on the Figure 1c, the aspect ratio is w/h = 50 μm/3 μm ≈ 16. For k = 0.75, ΔP = 5 Mpa, C = 10 MPa [*Ozkaya*, 1988], equation (1) indicates that lateral fracturing may occur if the vertical stress S_v is lower than 116 MPa, which corresponds to a depth h smaller than 4000 m.

[31] One limitation of this calculation is the assumption that the kerogen patches are surrounded by impermeable rock. In reality, shales have very small permeabilities and the transformation reaction is slow. The generated fluids may migrate through the rock matrix without producing pressure gradients that are large enough to cause fracturing. However, magma emplacement in sedimentary basins may result in much higher maturation rates and the rapid production of hydrocarbon fluids may cause rapid internal pressure build up and fracture generation.

[32] To summarize our observations, correlation analysis monitoring of the deformation of the sample indicated abrupt swelling perpendicular to the bedding just before cracks formation began. Petrography observations showed that the main cracks initiate in the finer grained clay-rich layers where a higher amount of organic matter is present. Thermogravimetry and gas chromatography analyses showed that the sample began to lose significant mass and release water, CO_2 and hydrocarbon gasses at about 350°C. These observations support a scenario in which the kerogen, present in thin lenses, starts to decompose around 350°C, causing volume increase and internal pressure build up leading to fracturing. The fracturing mechanism observed experimentally, including crack formation and crack geometry, was successfully reproduced by a 2D "fiber-bundle" lattice simulation. The success of the statistical fracture model indicates that material disorder and local elastic interactions play a key role in the development of the observed percolation like fracture. The implication is that percolating low permeability fluid pathways are formed in the shale long before macroscopic fracturing occurs.

[33] In the present study we do not characterize fracturing of source rocks under natural conditions. In particular, no confinement was applied to the sample. We therefore suggest that the results of our experiments can be directly relevant to better understand induced fracturing of shales located at shallow depth or outcrops, where the confinement pressure is low. More generally, the methods developed here will be relevant for future studies under more realistic conditions.

[34] **Acknowledgments.** We acknowledge support by the Petromaks program of the Norwegian Research Council. We thank Elodie Boller at ESRF for her help during the tomography scans and Rodica Chiriac for her help with the thermogravimetry analyses. This study was supported by a Center of Excellence grant from the Norwegian Research Council to the Physics of Geological Processes Center (PGP).

References

Alava, M. J., P. K. V. V. Nukalaz, and S. Zapperi (2006), Statistical models of fracture, *Adv. Phys.*, *55*, 349–476, doi:10.1080/00018730300741518.

Berg, R. R., and A. F. Gangi (1999), Primary migration by oil-generation microfracturing in low-permeability source rocks: Application to the Austin Chalk, Texas, *AAPG Bull.*, *83*, 727–756.

Bjørlykke, K. (2010), *Petroleum Geoscience: From Sedimentary Environments to Rock Physics*, Springer, Berlin, Germany.

Bornert, M., F. Vales, H. Gharbi, and D. N. Minh (2010), Multiscale full-field strain measurements for micromechanical investigations of the hydromechanical behaviour of clayey rocks, *Strain*, *46*, 33–46.

Capuano, R. M. (1993), Evidence of fluid flow in microcracks in geopressured shales, *AAPG Bull.*, *77*, 1303–1314.

Grebowicz, J. (2008), Thermal properties of Green River oil shales, *Geol. Soc. Am. Abstr. Programs*, *40*, 554.

Hild, F., and S. Roux (2006), Digital image correlation: From displacement measurement to identification of elastic properties: A review, *Strain*, *42*, 69–80, doi:10.1111/j.1475-1305.2006.00258.x.

Jensen, H. B. (1979), Oil shale in situ research and development, Talley Energy systems final report, DOE/LC/01791–T1, U.S. Dep. of Energy, Washington, D. C.

Jin, Z.-H., S. E. Johnson, and Z. Q. Fan (2010), Subcritical propagation and coalescence of oil-filled cracks: Getting the oil out of low-permeability source rocks, *Geophys. Res. Lett.*, *37*, L01305, doi:10.1029/2009GL041576.

Jung, H. (2004), Intermediate-depth earthquake faulting by dehydration embrittlement with negative volume change, *Nature*, *428*(6982), 545–549, doi:10.1038/nature02412.

Lash, G. G., and T. Engelder (2005), An analysis of horizontal microcracking during catagenesis: Example from Catskill delta complex, *AAPG Bull.*, *89*, 1433–1449, doi:10.1306/05250504141.

Littke, R., D. R. Baker, and D. Leythaeuser (1988), Microscopic and sedimentologic evidence for the generation and migration of hydrocarbons in Toarcian source rocks of different maturities, *Org. Geochem.*, *13*, 549–559, doi:10.1016/0146-6380(88)90075-7.

Marquez, X. M., and E. W. Mountjoy (1996), Microcracks due to overpressure caused by thermal cracking in well-sealed Upper Devonian reservoirs, deep Alberta basin, *AAPG Bull.*, *80*, 570–588.

Mazzini, A. (2009), Mud volcanism: Processes and implications, *Mar. Pet. Geol.*, *26*, 1677–1680, doi:10.1016/j.marpetgeo.2009.05.003.

Obara, K. (2002), Nonvolcanic deep tremor associated with subduction in southwest Japan, *Science*, *296*, 1679–1681, doi:10.1126/science.1070378.

Olson, W. A. (1980), Stress relaxation in oil shale, in *Proceedings of 21st Symposium on Rock Mechanics*, edited by D. A. Summers, pp. 517–520, Univ. of Miss., Rolla.

Ozkaya, I. (1988), A simple analysis of oil-induced fracturing in sedimentary rocks, *Mar. Pet. Geol.*, *5*, 293–297, doi:10.1016/0264-8172(88)90008-6.

Pradhan, S., A. Hansen, and B. K. Chakrabarti (2010), Failure processes in elastic fiber bundles, *Rev. Mod. Phys.*, *82*, 499–555, doi:10.1103/RevModPhys.82.499.

Rechenmacher, A. L., and R. J. Finno (2004), Digital image correlation to evaluate shear banding in dilative sands, *Geotech. Test. J.*, *27*, 13–22, doi:10.1520/GTJ10864.

Røyne, A., B. Jamtveit, J. Mathiesen, and A. Malthe-Sorrenssen (2008), Controls of rock weathering rates by reaction-induced hierarchical fracturing, *Earth Planet. Sci. Lett.*, *275*, 364–369, doi:10.1016/j.epsl.2008.08.035.

Ruble, T. E., M. D. Lewan, and R. P. Philp (2001), New insights on the Green River petroleum system in the Uinta basin from hydrous pyrolysis experiments, *AAPG Bull.*, *85*, 1333–1371.

Smith, J. W., and K. P. Chong (1984) Introduction to mechanics of oil shale, in *Mechanics of Oil Shale*, edited by K. P. Chong and J. W. Smith, pp. 1–41, Elsevier, New York.

Sonka, M., V. Hlavac, and R. Boyle (1999), *Image Processing, Analysis and Machine Vision*, PWS Publ., Pacific Grove, Calif.

Svensen, H., S. Planke, A. Malthe-Sorenssen, B. Jamtveit, R. Myklebust, T. R. Eidem, and S. S. Rey (2004), Release of methane from a volcanic basin as a mechanism for initial Eocene global warming, *Nature*, *429*(6991), 542–545, doi:10.1038/nature02566.

Thomas, H. E. (1972), Hydraulic Fracturing of Wyoming Green River Oil Shale: Field Experiments, *Phase I, Rep. Invest. Ser.*, vol. 7596, Bur. of Mines, U.S. Dep. of the Inter., Washington, D. C.

Vernik, L., and C. Landis (1996), Elastic anisotropy of source rocks: Implications for hydrocarbon generation and primary migration, *AAPG Bull.*, *80*, 531–544.

Viggiani, G. (2009), Mechanisms of localized deformation in geomaterials: An experimental insight using full-field measurement techniques, in *Mechanics of Natural Solids*, pp. 105–125, Springer, New York.

D. K. Dysthe, B. Jamtveit, M. Kobchenko, A. Malthe-Sørenssen, A. Mazzini, H. Panahi, and J. Scheibert, Physics of Geological Processes, University of Oslo, Oslo N-0316, Norway. (kobchenko.maya@gmail.com)

P. Meakin, Center for Advanced Modeling and Simulation, Idaho National Laboratory, PO Box 1625, MS 2211, Idaho Falls, ID 83415, USA.

F. Renard, Institut des Sciences de la Terre, Université Joseph Fourier, CNRS, Grenoble F-38041, France.